Unravelling the Role of Electric and Magnetic Dipoles in Biosensing with Si Nanoresonators

Ozlem Yavas[1], Mikael Svedendahl[1,2], Romain Quidant*[1,3]*

[1] ICFO - Institut de Ciències Fotòniques, The Barcelona Institute of Science and Technology, 08860 Castelldefels (Barcelona), Spain

[2] Department of Applied Physics, KTH Royal Institute of Technology, SE-114 19, Stockholm, Sweden

[3] ICREA - Institució Catalana de Recerca i Estudis Avançats, 08010 Barcelona, Spain

Keywords: silicon nanoresonators, Mie resonances, biosensing, lab-on-a-chip, dielectric nanophotonics, optical nanoresonators

Abstract: High refractive index dielectric nanoresonators are attracting much attention due to their ability to control both electric and magnetic components of light. Combining confined modes with reduced absorption losses, they have recently been proposed as an alternative to nanoplasmonic biosensors. In this context, we study the use of semi-random silicon nanocylinder arrays, fabricated with simple and scalable colloidal lithography for the efficient and reliable detection of biomolecules in biological samples. Interestingly, electric and magnetic dipole resonances are associated to two different transduction mechanisms: extinction decrease and resonance redshift, respectively. By contrasting both observables, we identify clear advantages in tracking changes in the extinction magnitude. Our data demonstrate

that, despite its simplicity, the proposed platform is able to detect prostate specific antigen (PSA) in human serum with limits of detection meeting clinical needs.

Rapid, highly sensitive and specific detection of biomolecules is a common goal for many applications including early diagnosis and treatment monitoring. In this context, emerging integrated biosensing platforms (also known as lab-on-chip, LOC) aim at developing point-of-care (POC) devices with reduced cost and ease of use.[1–3] Among the diversity of transduction schemes, optical biosensors hold great promises owing to a combination of advantages, including highly sensitive, rapid and label-free detection schemes, which are also compatible with microfluidic platforms.[4]

In particular, analyte detection using localized surface plasmon resonances (LSPR) in metallic nanoparticles has been extensively studied over the last decades[5–7] and more recently integrated into LOC platforms for parallel, multiplexed and sensitive biosensing applications.[8–10] Despite their highly confined electromagnetic modes, LSPR sensors suffer from dissipative losses that limit their optical quality factors and hence, their sensing performances.

High refractive index dielectric nanoparticles (HRDNs) have recently been suggested as a potential alternative to their metallic counterpart, due to their lower ohmic losses and highly tunable optical responses.[11–16] High refractive index dielectric materials have already contributed to cloaking,[17] super-lensing,[18] negative refractive index[19] and biosensing.[12,20,21] Light coupling with HRDNs result in both electric and magnetic multipole modes which can be engineered by controlling the nanostructure design.[22–24] The sensitivity of those resonance modes to their surrounding media has been recently shown to be an attractive and competing alternative to LSPR biosensors.[12,14,21,25–27]

Owing to its high refractive index, abundance, compatibility with microelectronics industry and well-developed fabrication processes, silicon is one of the most widely used materials for dielectric nanophotonics. It was theoretically and experimentally shown that the optical response of silicon nanostructures is highly sensitive to their surrounding environment.[12,26,28–33] First, silicon nanosphere dimers, fabricated by laser ablation, showed a broadening of their electric dipole modes upon increase of the surrounding refractive index.[12] More recently, Bontempi *et al.* reported on biotin-streptavidin detection with silicon nanodisk arrays, fabricated by electron beam lithography (EBL).[14] These recent efforts, both theoretical and experimental, suggest that Mie resonances in HRDNs have the potential to greatly benefit LOC technologies. As an important step towards this goal, EBL-processed periodic silicon nanodisk arrays were integrated into a state-of-the-art microfluidic chip to perform real-time detection of cancer biomarkers in human serum.[21] While at that stage, Si-based nano-optical sensors have already reached comparable performances to LSPR counterparts, further developments are required to fully exploit their potential. In particular, there is a need to further understand how the control over both electric and magnetic dipoles could benefit the detection sensitivity. Furthermore, especially within the context of point-of-care applications, one need to identify cost effective strategies to fabricate HRDN sensors over large areas.

Here, we present a platform which contributes to both objectives. A semi-random array of silicon nanocylinders (Si-NCs), fabricated by low-cost and scalable colloidal lithography, is integrated into a microfluidic environment to perform prostate specific antigen (PSA) detection through two different transduction mechanisms: resonance redshift and extinction reduction. Interestingly, we find these observables are associated to electric and magnetic dipole resonances, respectively. Through real-time tracking of both signals, we demonstrate that extinction reduction, mainly related to the electric dipole, leads to better sensing performances in our configuration.

Our sensing chip consists of a semi-random array of Si-NCs integrated into a microfluidic environment. Similar arrays have previously been used in a LSPR biosensing schemes.[34–38] Electric and magnetic dipole resonances of a Si-NC depend on the cylinder height and radius, as well as the surrounding media. In this study, we choose a Si-NC height of 130 nm, in order to support both electric and magnetic dipole resonances, as illustrated in Figure 1a. In order to determine the optimum radius of individual Si-NCs, we examine their refractive index sensitivity by numerical simulations using COMSOL FEM solver. Here, isolated Si-NCs are placed on a glass substrate and excited by linearly polarized light. In Figure1b, we study the extinction spectrum shift due to the change of the superstrate refractive index from 1.33 to 1.35. Figure 1b shows that 140 nm radius provides the highest sensitivity for resonance wavelengths below 1000 nm, which serves as the upper limit when using Si-based CCD cameras. As shown in Figure 1c, this optimum case corresponds to overlapping electric and magnetic dipole resonances that result in a single peak in the extinction spectrum.

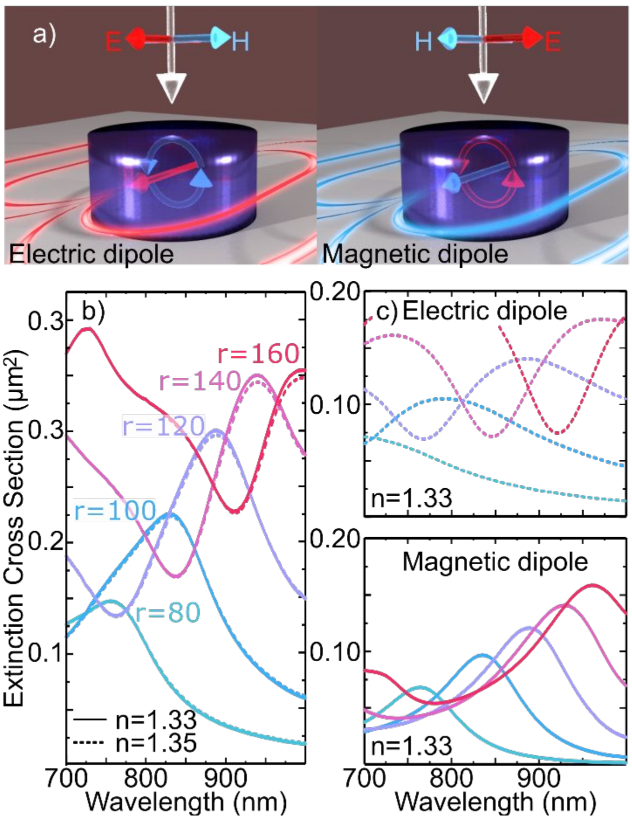

Figure 1. Numerical investigation of individual Si-NCs. a) 130 nm tall Si-NCs can support both (top) electrical and (bottom) magnetic dipolar resonances. b) The extinction cross section of 130 nm tall Si-NCs with varying radius, situated on a glass support surrounded by media with

either n = 1.33 or n = 1.35. c) The extinction cross section is mainly composed of (top) electrical and (bottom) magnetic dipolar modes.

In order to achieve fast, cheap and large-scale fabrication, we use colloidal lithography and fabricated semi-randomly distributed Si-NCs of height 130 nm and radius 140 nm with electric and magnetic dipole resonance at 900 nm in aqueous environment (Figure 2). We first coat Si-on-quartz substrates with 50 nm gold with 2 nm titanium adhesion layer. Then, we drop-cast sulfate latex beads of 0.2% w/v on the gold surface (Figure 2b). The beads are charged and therefore repel each other and form a semi-random array, that is, without any long-range order, but with a typical nearest neighbour distance.[39] We use them as a reactive ion etching mask for etching the gold layer with argon gas. Next, we remove the beads from the surface of the etched gold nanodisks by an adhesive tape (Figure 2c) and use the patterned gold mask for etching the silicon layer with RIE using SF_6 and C_4F_8 gases. Finally, we clean the substrate by piranha solution, which removes the gold mask layer by etching away the Ti layer below (for further details on the fabrication, see the Methods/Experimental section below).

The SEM image of the semi-randomly distributed Si-NCs are shown in Figure 2d. With this EBL-free method, the whole sample area can be patterned with nanostructures simultaneously without altering the fabrication time or cost. The areas on the substrate to be patterned can be selected by tape stripping the beads away before using them as an etch mask. More precise bead stripping method is described by Acimovic *et al.* for patterning the sample surface with precision of few micrometers using a homemade PDMS stripping tape.[40] For our sensing device, we tape strip the edges of the sample, leaving the NCs only at the central region of 0.5 cm^2 on the chip.

The extinction spectra of the semi-random Si-NC array measured in air and in water are shown in Figure 2e. The resonance position in air and in water was 870 and 900 nm, respectively, showing a clear redshift due to the large refractive index change of the local environment. Furthermore, the extinction amplitude is reduced in water compared to the spectrum in air, which is in-line with previous reports.[12,27,33]

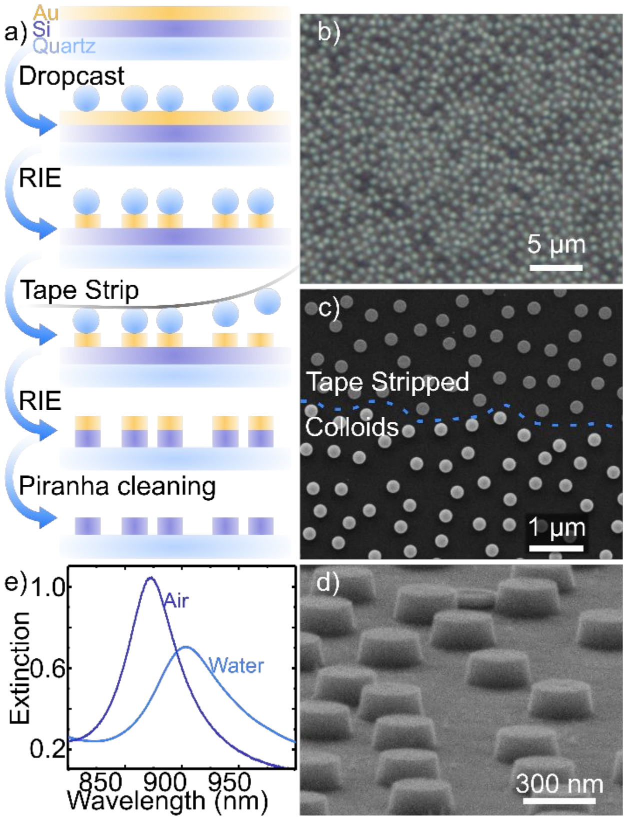

Figure 2: Semi-random silicon nanocylinder (Si-NC) arrays. (a) Fabrication steps of semi-random Si-NC arrays. (b) Dark field microscopy image of the sulfate latex beads dropcasted on the gold layer. (c) The SEM image of the substrate after the tape stripping step showing the stripped regions with gold nanodisks (above the dashed line) and unstripped regions with the beads on top of gold nanodisks (below the dashed line). (d) The SEM image of the Si-NCs on quartz after piranha cleaning of the substrate to remove the gold mask. (e) The measured extinction spectra of the silicon disks in air (black) and in water (grey).

To test the sensing performance of the fabricated Si-NC arrays, we integrate it into a multilayer microfluidic network of PDMS,[9] which enables the control of the sample flow on the sensing regions that are separated by microfluidic channels (Figure 3a). The eight distinct channels for sample detection are accessible by a common inlet or individually through different inlets on the chip, allowing parallel measurements, as illustrated in Figure 3b. The sample flow is controlled by regulating the pressure on the control network of the chip through electronic valves. By altering the pressure on the control channels, the micromechanical valves on the chip are opened and closed, enabling and disabling the flow of reagents and samples in the chip. The electronic valves are controlled by a custom software that is programmed to run complex operational steps automatically. The microfluidic chip design and the operation principles, as well as the fabrication procedure are described in Acimovic *et al*.[9] and Yavas *et al*.[21] This configuration is crucial for rapid and practical execution of complex immunoassay steps in a highly controlled environment.

Results/Discussions

Initially, we evaluate the bulk refractive index sensitivity (BRIS) of the Si-NCs by sequentially flowing different percentage glucose solutions through the channels and tracking the centroid position and the extinction amplitude. The centroid shift of the extinction peak with respect to the refractive index of the glucose solution is shown in Figure 3c-d. The semi-random Si-NC arrays exhibits a BRIS of 86 nm/RIU by the conventional centroid tracking method. Previously, periodic arrays of 50-nm high silicon nanodisks were showed to exhibit significantly higher BRIS value (227 nm/RIU), due to diffractive modes induced by the periodicity.[21] It is important to note that high BRIS value does not necessarily correspond to a lower limit of detection (LOD) in molecular sensing, as the mode volume and the spatial distribution of the BRIS also plays a crucial role in the biosensing performance.[41,42]

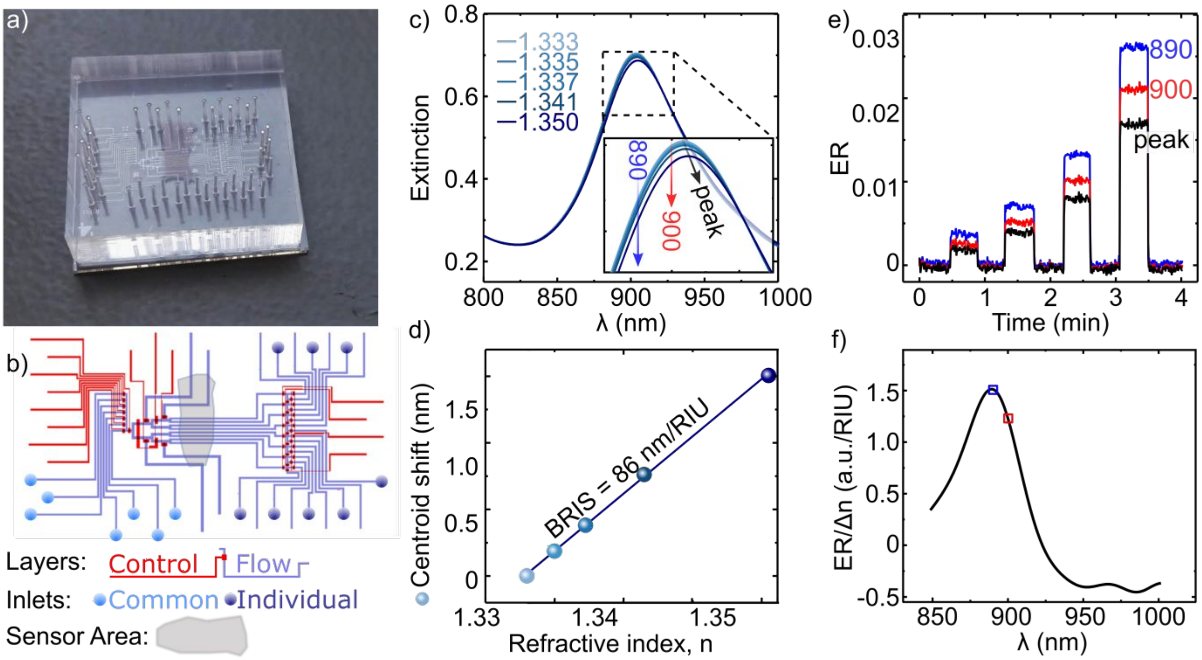

Figure 3: Sensing chip and the bulk refractive index sensitivity (BRIS). (a) A photograph of the integrated microfluidic chip. The sensor array in the middle of the chip is seen as a darker region below the channels. The chip is 25x25 mm with a thickness of 0.5 cm. (b) The microfluidic flow (blue) and control (red) channel network with Si-NC array aligned with 8 sensing channels. The fluids can be flown into all the 8 channels through a common inlet (yellow), or individually through individual inlets (green). Unlabelled blue channels are the waste outlets of the chip. (c) The extinction spectra of the sensors in glucose solutions of varying concentrations. (d) The respective centroid shifts from (c). The slope of the linear response of centroid position to changing refractive index is the BRIS. (e) The real time traces of the extinction amplitude response to changing refractive index by sequential flow of different percentage glucose concentrations. The inset shows the wavelength positions the three measurements: the peak wavelength (black line), at 900 nm (red line) and at 890 nm (blue line). (f) The extinction reduction sensitivity as a function of wavelength. The extinction reduction (ER) is the negative change of extinction signal with respect to the refractive index. The highest sensitivity was reached at 890 nm (blue). The change in extinction with respect to the refractive

index, n, of the surrounding medium is shown in the inset for 890 nm, 900 nm and at the peak position of the extinction.

In addition to the centroid shift, we notice that the extinction is reduced while increasing the surrounding refractive index, as seen in Figure 3c. Based on this observation, we evaluate the sensing performance of our sensors by tracking the extinction reduction in Figure 3e-f. We define extinction reduction as the negative change in the extinction signal. In Figure 3e, the real-time response of the extinction amplitude to the sequential flow of the distinct glucose concentrations, with washing steps in between, is presented for three different cases. We show the extinction amplitude change at the peak maxima, at 900 nm and at 890 nm, exhibiting a linear dependence to the refractive index. The whole wavelength range scanned for the maximum extinction reduction sensitivity is shown in Figure 3f, which shows that at 890 nm the sensitivity is the highest. These results suggest that detection could be performed by monitoring the extinction amplitude at a defined wavelength (without the need for measuring the entire extinction spectrum), hence strongly simplifying the optical set-up.

To back up our experimental observations and study the origin behind the two different transduction mechanisms, we performed extensive numerical simulations using COMSOL FEM solver (See SI for the semi-analytical calculations by island film theory[16,43]). First, we simulated and compared the single and ensemble of Si-NCs. Figure 4a and c show the resonances of an isolated silicon Si-NC in aqueous solution while Figure 4b and d demonstrate a small part of a semi-random array of Si-NCs under identical conditions. As seen in Figure 4a, the resonance position of an isolated Si-NC redshifts and the extinction amplitude decreases as the surrounding refractive index increases. However, this effect is enhanced as more Si-NCs are assembled in a semi-random array. As can be seen in Figure 4f, the resonance shift for the array is about twice larger than for an isolated Si-NC. Also, the extinction reduction is increased by a similar amount (Figure 4g). These results are likely due to increased shielding effects on the interparticle electromagnetic coupling induced by the increased refractive index of the surrounding medium. While plasmonic metal nanostructures in similar arrangements have shown negligible coupling,[43] the mode extension for Si-NCs is significantly greater.[21] Furthermore, due to limited computation power, we only modelled 10 nanostructures in the semi-random array assembly. We foresee the observed effects to increase further in larger arrays, reducing the mismatch with experimental observations.

For the parameters of the fabricated Si-NCs, both magnetic and electric fields are enhanced at resonance. Interestingly, by separating the extinction cross section into electric and magnetic dipolar components (Figure 4e), the underlying mechanisms behind resonance shift and extinction reduction can be unveiled. From Figure 4f and g, it appears that the magnetic resonance is responsible for the resonance redshift, while the extinction reduction is related to the electrical dipole. This observation explains the sources of the experimentally observed resonance redshift and extinction reduction reported above.

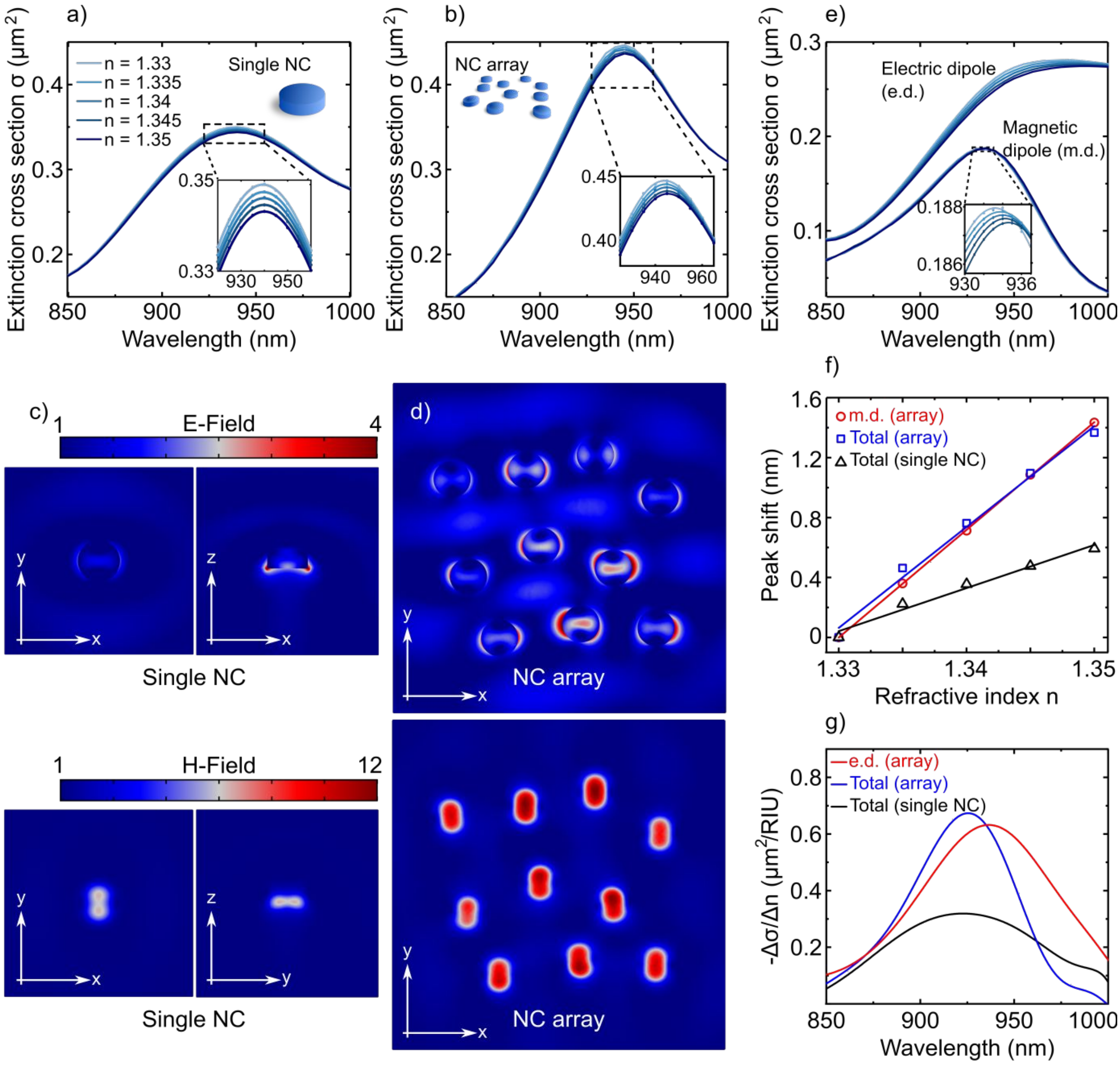

Figure 4: FEM simulations of Si-NCs. The extinction cross section of (a) a single Si-NC and (b) the average response from a semi-random Si-NC array of 10 particles, surrounded by media with different refractive indices. The E-field and H-field enhancements of (c) the single Si-NC and (d) the semi-random Si-NC array, around the resonance wavelength (940 nm). (e) The electric and magnetic dipolar (e.d. and m.d.) components of the extinction cross section of the Si-NC array. (f) The extinction peak shifts due to changing refractive index of surrounding medium. The m.d. resonance of the Si-NC array (red circles) and the total extinction of the Si-NC array (blue squares) and total extinction of a single Si-NC (black triangles) are analysed

and compared separately. (g) The wavelength dependence of the extinction cross section reduction (ER_σ) due to changing refractive index.

Finally, in order to demonstrate the biomolecule detection capability of our platform and compare both aforementioned transduction mechanisms, we focused on the detection of prostate specific antigen, PSA. PSA is a protein cancer marker whose concentration in serum tends to overpass its normal level (4-10 ng/ml) for patients affected by prostate cancer.[44,45] The sandwich immunoassay scheme we use is sketched in Figure 5a. The binding events are observed in real-time as a redshift of the resonance centroid and a reduction of the extinction. First, a selective monoclonal capture antibody for PSA is immobilized on the sensor surface in all eight channels, through passive adsorption, as in enzyme linked immunosorbent assay (ELISA). Then, through individual inlets, eight calibration samples in PBS-BSA (Phosphate Buffer Saline-Bovine Serum Albumin, 1%) buffer with different PSA concentrations is flowed into the distinct channels and the PSA is captured by the antibody on sensor surface, leading to additional adsorption signals. One of the eight channels was used as a control channel, with only PBS-BSA(1%) buffer flowing and no PSA. Following the PSA capture step, a polyclonal antibody is then introduced in all channels as an amplification antibody, binding to PSA, resulting in larger and more detectable signals as well as a higher selectivity of the assay. Each step of the sandwich assay is adjusted to be 1 hour to have saturated signal shifts in each channel.

The PSA calibration curves obtained by tracking the resonance centroid redshift and by tracking the extinction reduction at 890 nm are displayed in Figure 5b and c, respectively. The control channel shows no binding signal, suggesting a high specificity. The limit of detection (LOD), calculated conventionally as the EC10 value of the four-parameter logistic curve fit, reached by centroid shift tracking was 1.55 ng/ml, which is below the clinical cut-off concentration of PSA for prostate cancer detection (4-10 ng/ml). Interestingly, the LOD reached by extinction reduction analysis of the same data is 0.83 ng/ml, outperforming the conventional centroid tracking method as well as the well-developed LSPR counterpart.[9]

Beyond the LOD, another relevant parameter for diagnostics purposes is the dynamic range of the calibration curves (EC20-EC80 range), determining the operating ranges of the sensor (shaded regions in Figure 5). The dynamic range for the centroid shift-based curve is 2.35 – 9.79 ng/ml, while the dynamic range for the extinction reduction-based curve extends over 1.87 – 30.0 ng/ml. While both calibration curves are within the clinically relevant range, the extinction reduction-based sensing offers a higher dynamic range and a smaller LOD, which is beneficial for diagnostic applications. Error bars in Figure 5 represent the replicas of the measurements on the same chip. The coefficient of variation (CV) for replicated measurements is between 1.1% and 16.3% for centroid shifts and 0.7% and 25.9% for extinction reduction.

We conclude that the electric dipolar mode, which dominates the extinction reduction mechanism, exhibits a better biomolecular sensing performance. This result is due to the higher exposure of the electrical mode to the surrounding medium. The magnetic dipolar modes are highly confined inside the Si-NCs, resulting in smaller sensitivity to changes at the Si-NC vicinity.

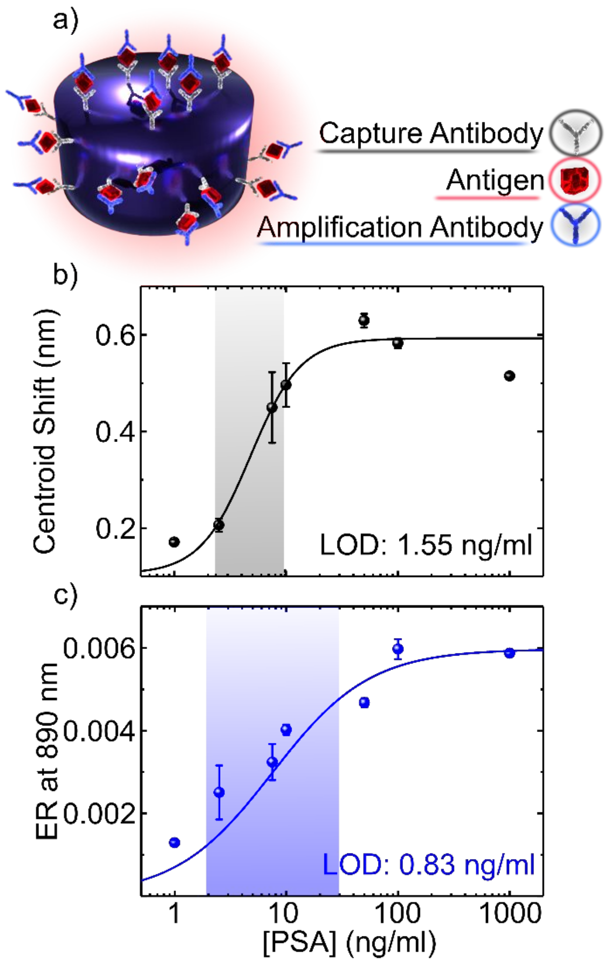

Figure 5: PSA detection results. (a) The sketch of the sandwich assay steps for antigen detection. First the capture antibody is immobilized on the sensor surface by passive adsorption (i), then the antigen is captured by the capture antibody (ii) and finally the signal is amplified by an amplification antibody (iii). (b-c) The calibration curve by the (b) centroid shifts and (c) extinction reduction due to the amplification antibody step obtained from the eight channels of the chip. Error bars represents the replicas of the measurement on the same chip.

Additionally, we have also calculated the total extinction reduction for the same measurement, by integrating the extinction peak over a wavelength range where the reduction is dominant, in order visualize the performance using a broadband illumination and detection scheme. Between 840 nm and 920 nm, the extinction reduction of the integrated signal lead to a very similar calibration curve for the PSA detection with LOD of 0.83 ng/ml (data shown in supporting information, Figure SI 3), offering a possibility of even cheaper and simpler excitation and detection schemes. This result suggests that a LED light source and a simple CCD camera or photodiode can be employed for excitation and readout, simplifying and reducing the cost of the set-up and providing the opportunity for an efficient POC platform to be developed.

PSA detection results demonstrate that on-chip sensing performance of partially randomized Si-NC arrays are competitive with their LSPR based counterparts.[21] Interestingly, the EBL-free and scalable sensor fabrication combined with the simplicity of the surface chemistry based on passive adsorption, suggest Si-NC arrays as a cost effective solution. Possibilities for resonance mode tuning for obtaining higher sensitivities, leaves room for improvement of such sensors.

Conclusions

In conclusion, we have demonstrated on-chip cancer marker detection using semi-randomized Si-NC arrays, employing the electric and magnetic dipole resonances for sensing, with low LOD and clinically relevant operating ranges. The proposed geometry allowed us to isolate the biosensing performance of Mie resonances, eliminating the contribution of Bragg modes involved in our previous work.[21] Two transduction mechanisms were studied and compared; extinction reduction that was associated to the electric dipolar mode and the resonance redshift mostly governed by the magnetic mode. Our PSA detection results show that the electric dipole mode, which is more exposed to the surrounding media, outperforms the magnetic mode. Interestingly, tracking the extinction reduction at a fixed wavelength could enable cheaper and simpler, spectroscopy-free, read-out, highly relevant to POC applications.

Methods/Experimental

Fabrication of Si-NC arrays - Semi-randomly distributed silicon nanoresonators are fabricated through a customized colloidal lithography technique. The 130 nm Si coated quartz substrates (25 x25 mm^2) were purchased from Siegert Wafer, GmbH. After cleaning the substrates, they are coated with an adhesion layer of 2 nm of Ti layer and 50 nm of Au. The sample is then treated with O_2 plasma for 5 s at 100 Watts (200 ml/min flow). Subsequently, the sample is incubated for 1 minute in 0.2% Poly-diallyl dimethylammonium chloride (PDDA) solution for surface activation, making the surface positively charged, and then washed with water and dried with N_2. After the surface activation step, the sample becomes ready for the drop-casting of sulfate-stabilized (negatively charged) latex beads (Thermofisher, S37491, 0.2 μm). 0.2% w/v solution of beads is dropcasted on the substrate, covering the whole surface, and after 1 minute, the surface was quickly rinsed with water and dried with N_2. In our sensing experiment, we removed the beads around the edges of the sample, using a scotch tape, leaving the beads only in the center of the substrate, which will be integrated with microfluidics and optically interrogated for sensing. The Au layer, masked by the beads, is etched by Ar gas (40 sccm) for 3 min 20 s in a reactive ion etching (RIE) chamber. The beads are then removed by tape stripping and the Au nanodisks used as a mask for etching the Si layer in RIE with C_4F_8 (70 sccm) and SF_6 (45 sccm), for 8 min. Finally, the sample is washed in piranha solution, which lifts off the Au layer by etching the underneath Ti layer and cleans the silicon nanodisk surface. The final radius and the density of the silicon nanodisks are 140 nm and 2.1 disks/μm^2.

Preparation of PDMS chips - The PDMS chips are fabricated using multilayer soft lithography technique. The silicon wafer molds are fabricated by UV-lithography, using photoresist, AZ9260 (Allresist, Gmbh). The dimensions and the design of the microfluidic channels are the same as in our previous works.[8,21] The PDMS flow and control layers are prepared in respective ratios of 1:5 and 1:10 polymer to curing agent. The flow layer is spin coated on the flow mold to achieve the membrane micromechanical valves. The control layer is molded on the control mold to achieve 0.5 cm of chip thickness. The PDMS is cured for 1 hour at 80 degrees. The PDMS is peeled off and the holes are punched to provide access to the channels. Two layers are aligned and bonded with the UV-Ozone plasma of 3 minutes. The final chips are baked at 80 degrees for 10 hours before they are bond with the substrate with sensors. Once the sensors are cleaned in 1:3 piranha solution, they are aligned and bond with the PDMS chips, which are surface activated by 3 minutes of UV-Ozone plasma. The integrated chip is then baked at 50 degrees for 10 hours before use.

Numerical Simulations - Simulations using the finite elements method were performed in Comsol 5.3a. The refractive index of Silicon was taken from experimental values (Figure S1), the refractive index of the substrate was set to 1.45 and the ambient refractive index was varied between 1.33 and 1.35. For the semi-random simulations, the respective positions of 10 nanocylinders were collected from SEM images of the fabricated samples and inserted into the simulation geometry. The electric ($\overline{p}$) and magnetic ($\overline{m}$) dipole moments were calculated from the numerically solved electrical fields:

$$\overline{p} = \int_V \varepsilon_0(\varepsilon(\overline{r}) - \varepsilon_1)\overline{E}(\overline{r})d\overline{r}$$

$$\overline{m} = \frac{-i\omega}{2}\int_V \varepsilon_0(\varepsilon(\overline{r}) - \varepsilon_1)\overline{r} \times \overline{E}(\overline{r})d\overline{r},$$

where ω is the radial frequency of light, $\overline{E}(\overline{r})$ is the electric field at position ($\overline{r}$), and ε and ε_1 are the permittivities of the nanostructure and the ambient, respectively.

ASSOCIATED CONTENT

Supporting Information available online

Contents: method for fabricating the semi-random Si-NC arrays, Semi-anaytical calculations and total extinction reduction analysis. Figures SI 1-3

AUTHOR INFORMATION

Corresponding Author:

*Mikael Svedendahl (svedend@kth.se)

*Romain Quidant (romain.quidant@icfo.eu)

Author Contributions:

O.Y. and M.S. planned the fabrication and experiment stages. O.Y. performed the fabrication of sensors, microfluidic chips and biosensing experiments. M.S. performed the simulations and interpreted the data. M.S and R.Q lead the project together. All authors wrote the manuscript together.

ACKNOWLEDGEMENT

The authors acknowledge financial support from the European Community's Seventh Framework Program under grant QnanoMECA (64790), Fundació Privada Cellex, and the Spanish Ministry of Economy and Competitiveness, through the "Severo Ochoa" Programme for Centres of Excellence in R&D (SEV-2015-0522) and grant FIS2016-80293-R, and Swedish Research Council (637-2014-6894).

REFERENCES

(1) Kozel, T. R.; Burnham-Marusich, A. R. Point-of-Care Testing for Infectious Diseases :

Past , Present , and Future. *J. Clin. Microbiol.* **2017**, *55*, 2313–2320.

(2) Tokel, O.; Inci, F.; Demirci, U. Advances in Plasmonic Technologies for Point of Care Applications. *Chem. Rev.* **2014**, *114*, 5728–5752.

(3) Chin, C. D.; Linder, V.; Sia, S. K. Lab on a Chip Commercialization of Microfluidic Point-of-Care Diagnostic Devices. *Lab Chip* **2012**, *12*, 2118–2134.

(4) Spindel, S.; Sapsford, K. E. Evaluation of Optical Detection Platforms for Multiplexed Detection of Proteins and the Need for Point-of-Care Biosensors for Clinical Use. *Sensors* **2014**, *14*, 22313–22341.

(5) Cao, J.; Sun, T.; Grattan, K. T. V. Gold Nanorod-Based Localized Surface Plasmon Resonance Biosensors: A Review. *Sensors Actuators, B Chem.* **2014**, *195*, 332–351.

(6) Unser, S.; Bruzas, I.; He, J.; Sagle, L. Localized Surface Plasmon Resonance Biosensing: Current Challenges and Approaches. *Sensors* **2015**, *15*, 15684–15716.

(7) Hammond, J.; Bhalla, N.; Rafiee, S.; Estrela, P. Localized Surface Plasmon Resonance as a Biosensing Platform for Developing Countries. *Biosensors* **2014**, *4*, 172–188.

(8) Yavas, O.; Acimovic, S. S.; Garcia-Guirado, J.; Berthelot, J.; Dobosz, P.; Sanz, V.; Quidant, R. Self-Calibrating on-a-Chip LSPR Sensing for Quantitative and Multiplexed Detection of Cancer Markers in Human Serum. *ACS Sensors* **2018**, *3*, 1376–1384.

(9) Aćimović, S. S.; Ortega, M. a.; Sanz, V.; Berthelot, J.; Garcia-Cordero, J. L.; Renger, J.; Maerkl, S. J.; Kreuzer, M. P.; Quidant, R. LSPR Chip for Parallel, Rapid, and Sensitive Detection of Cancer Markers in Serum. *Nano Lett.* **2014**, *14*, 2636–2641.

(10) Chen, P.; Chung, M. T.; Mchugh, W.; Nidetz, R.; Li, Y.; Fu, J.; Al, C. E. T. Multiplex Serum Cytokine Immunoassay Using Nanoplasmonic Biosensor Microarrays. *ACS*

Nano **2015**, *9*, 4173–4181.

(11) Krasnok, A.; Makarov, S.; Petrov, M.; Savelev, R.; Belov, P.; Kivshar, Y. Towards All-Dielectric Metamaterials and Nanophotonics. *SPIE Opt. Optoelect.* **2015**, *9502*, 950203–950203.

(12) Yan, J.; Liu, P.; Lin, Z.; Yang, G. New Type High-Index Dielectric Nanosensors Based on the Scattering Intensity Shift. *Nanoscale* **2016**, *8*, 5996–6007.

(13) Regmi, R.; Berthelot, J.; Winkler, P. M.; Mivelle, M.; Proust, J.; Bedu, F.; Ozerov, I.; Begou, T.; Lumeau, J.; Rigneault, H.; Garcia-Parajo, M. F.; Bidault, S.; Wenger, J.; Bonod, N. All-Dielectric Silicon Nanogap Antennas to Enhance the Fluorescence of Single Molecules. *Nano Lett.* **2016**, *16*, 5143–5151.

(14) Bontempi, N.; Chong, K. E.; Orton, H. W.; Staude, I.; Choi, D.-Y.; Alessandri, I.; Kivshar, Y. S.; Neshev, D. N. Highly Sensitive Biosensors Based on All-Dielectric Nanoresonators. *Nanoscale* **2017**, *9*, 4972–4980.

(15) Kuznetsov, A. I.; Miroshnichenko, A. E.; Brongersma, M. L.; Kivshar, Y. S.; Luk'yanchuk, B. Optically Resonant Dielectric Nanostructures. *Science (80-.).* **2016**, *354*, aag2472.

(16) Odebo Länk, N.; Verre, R.; Johansson, P.; Käll, M. Large-Scale Silicon Nanophotonic Metasurfaces with Polarization Independent Near-Perfect Absorption. *Nano Lett.* **2017**, *17*, 3054–3060.

(17) Alitalo, P.; Tretyakov, S. Electromagnetic Cloaking with Metamaterials. *Mater. Today* **2009**, *12*, 22–29.

(18) Pendry, J. B. Negative Refraction Makes a Perfect Lens. *Phys. Rev. Lett.* **2000**, *85*,

3966–3969.

(19) Soukoulis, C. M.; Linden, S.; Wegener, M. Negative Refractive Index at Optical Wavelengths. **2007**, *315*, 47–50.

(20) Tittl, A.; Leitis, A.; Liu, M.; Yesilkoy, F.; Choi, D.-Y.; Neshev, D. N.; Kivshar, Y. S.; Altug, H. Imaging-Based Molecular Barcoding with Pixelated Dielectric Metasurfaces. *Science (80-.).* **2018**, *360*, 1105–1109.

(21) Yavas, O.; Svedendahl, M.; Dobosz, P.; Sanz, V.; Quidant, R. On-a-Chip Biosensing Based on All-Dielectric Nanoresonators. *Nano Lett.* **2017**, *17*, 4421–4426.

(22) Staude, I.; Miroshnichenko, A. E.; Decker, M.; Fofang, N. T.; Liu, S.; Gonzales, E.; Dominguez, J.; Luk, T. S.; Neshev, D. N.; Brener, I.; Kivshar, Y. Tailoring Directional Scattering through Magnetic and Electric Resonances in Subwavelength Silicon Nanodisks. *ACS Nano* **2013**, *7*, 7824–7832.

(23) Afridi, A.; Canet-ferrer, J.; Philippet, L.; Osmond, J.; Berto, P.; Quidant, R. Electrically Varifocal Silicon Metalens. *ACS Photonics* **2018**, *5*, 4497–4503.

(24) Yu, Y. F.; Zhu, A. Y.; Fu, Y. H.; Luk, B.; Kuznetsov, A. I. High-Transmission Dielectric Metasurface with 2 π Phase Control at Visible Wavelengths. *Laser and Photonics Reviews* **2015**, *418*, 412–418.

(25) Yang, Y.; Kravchenko, I. High Quality Factor Fano-Resonant All-Dielectric Metamaterials. *Arxiv* **2014**, 1–16.

(26) Semouchkina, E.; Duan, R.; Semouchkin, G.; Pandey, R. Sensing Based on Fano-Type Resonance Response of All-Dielectric Metamaterials. *Sensors* **2015**, *15*, 9344–9359.

(27) García-Cámara, B.; Gómez-Medina, R.; Saenz, Jose, J.; Sepulveda, B. Sensing with

Magnetic Dipolar Resonances in Semiconductor Nanospheres. *Opt. Express* **2013**, *21*, 23007–23020.

(28) Schmid, J. H.; Sinclair, W.; García, J.; Janz, S.; Lapointe, J.; Poitras, D.; Li, Y.; Mischki, T.; Lopinski, G.; Cheben, P.; Delâge, a; Densmore, a; Waldron, P.; Xu, D.-X. Silicon-on-Insulator Guided Mode Resonant Grating for Evanescent Field Molecular Sensing. *Opt. Express* **2009**, *17*, 18371–18380.

(29) Evlyukhin, A. B.; Reinhardt, C.; Seidel, A.; Luk'Yanchuk, B. S.; Chichkov, B. N. Optical Response Features of Si-Nanoparticle Arrays. *Phys. Rev. B - Condens. Matter Mater. Phys.* **2010**, *82*, 1–12.

(30) Chong, K. E.; Hopkins, B.; Staude, I.; Miroshnichenko, A. E.; Dominguez, J.; Decker, M.; Neshev, D. N.; Brener, I.; Kivshar, Y. S. Observation of Fano Resonances in All-Dielectric Nanoparticle Oligomers. *Small* **2014**, *10*, 1985–1990.

(31) Habteyes, T. G.; Staude, I.; Chong, K. E.; Dominguez, J.; Decker, M.; Miroshnichenko, A.; Kivshar, Y.; Brener, I. Near-Field Mapping of Optical Modes on All-Dielectric Silicon Nanodisks. *ACS Photonics* **2014**, *1*, 794–798.

(32) Zhang, J.; MacDonald, K. F.; Zheludev, N. I. Near-Infrared Trapped Mode Magnetic Resonance in an All-Dielectric Metamaterial. *Opt. Express* **2013**, *21*, 26721.

(33) Evlyukhin, A. B.; Novikov, S. M.; Zywietz, U.; Eriksen, R. L.; Reinhardt, C.; Bozhevolnyi, S. I.; Chichkov, B. N. Demonstration of Magnetic Dipole Resonances of Dielectric Nanospheres in the Visible Region. *Nano Lett.* **2012**, *12*, 3749–3755.

(34) Feuz, L.; Jonsson, M. P.; Höök, F. Material-Selective Surface Chemistry for Nanoplasmonic Sensors: Optimizing Sensitivity and Controlling Binding to Local Hot Spots. *Nano Lett.* **2012**, *12*, 873–879.

(35) Dahlin, A. B.; Chen, S.; Jonsson, M. P.; Gunnarsson, L.; Käll, M.; Höök, F. High-Resolution Microspectroscopy of Plasmonic Nanostructures for Miniaturized Biosensing. *Anal. Chem.* **2009**, *81*, 6572–6580.

(36) Wersäll, M.; Verre, R.; Svedendahl, M.; Johansson, P.; Käll, M.; Shegai, T. Directional Nanoplasmonic Antennas for Self-Referenced Refractometric Molecular Analysis. *J. Phys. Chem. C* **2014**, *118*, 21075–21080.

(37) Chen, S.; Svedendahl, M.; Duyne, R. P. V.; Käll, M. Plasmon-Enhanced Colorimetric ELISA with Single Molecule Sensitivity. *Nano Lett.* **2011**, *11*, 1826–1830.

(38) Svedendahl, M.; Verre, R.; Käll, M. Refractometric Biosensing Based on Optical Phase Flips in Sparse and Short-Range-Ordered Nanoplasmonic Layers. *Light Sci. Appl.* **2014**, *3*, e220.

(39) Fredriksson, H.; Alaverdyan, Y.; Dmitriev, A.; Langhammer, C.; Sutherland, D. S.; Zäch, M.; Kasemo, B. Hole-Mask Colloidal Lithography. *Adv. Mater.* **2007**, *19*, 4297–4302.

(40) Acimovic, S. S.; Šípová, H.; Emilsson, G.; Dahlin, A. B.; Antosiewicz, T. J.; Käll, M. Superior LSPR Substrates Based on Electromagnetic Decoupling for On-a-Chip High-Throughput Label-Free Biosensing. *Light Sci. Appl.* **2017**, *6*, 1–8.

(41) Svedendahl, M.; Chen, S.; Dmitriev, A.; Kall, M. Refractometric Sensing Using Propagating *versus* Localized Surface Plasmons: A Direct Comparison. *Nano Lett.* **2009**, *9*, 4428–4433.

(42) Aćimović, S. S.; Kreuzer, M. P.; González, M. U.; Quidant, R. Plasmon Near-Field Coupling in Metal Dimers as a Step toward Single-Molecule Sensing. *ACS Nano* **2009**, *3*, 1231–1237.

(43) Svedendahl, M.; Käll, M. Fano Interference between Localized Plasmons and Interface Reflections. *ACS Nano* **2012**, *6*, 7533–7539.

(44) Brawer, MK. Chetner, MP. Beatie, J. Buchner, DM. Vessella, RL. Lange, P. Screening for Prostatic Carcinoma with Prostate Specific Antigen. *J. Urol.* **1992**, *147*, 841–845.

(45) Catalona, W. J., J. P. Richie, F. R. Ahmann, M. A. Hudson, P. T. Scardino, R. C. Flanigan, J. B. deKernion. Comparison of DRE and Serum PSA in the Early Detection of Prostate Cancer: Results of a Multicenter Clinical Trial of 6630 Men. *J. Urol.* **1994**, *151*, 1283–1290.

TOC Figure: